frontiers | Frontiers in Detector Science and Technology

TYPE Original Research
PUBLISHED 13 August 2025
DOI 10.3389/fdest.2025.1614781

OPEN ACCESS

EDITED BY
Gabriele Croci,
University of Milano-Bicocca, Italy

REVIEWED BY
Francesc Monrabal Capilla,
Donostia International Physics Center (DIPC), Spain
Piet Verwilligen,
National Institute for Nuclear Physics of Bari, Italy

*CORRESPONDENCE
C. A. O. Henriques,
henriques@uc.pt

RECEIVED 19 April 2025
ACCEPTED 14 July 2025
PUBLISHED 13 August 2025

CITATION
Henriques CAO, Fernandes LMP, Silva PAOC, González-Díaz D, Azevedo CDR, Santos JMFd and Monteiro CMB (2025) Experimental characterization of electron transport and electroluminescence in xenon-molecular mixtures.
Front. Detect. Sci. Technol. 3:1614781.
doi: 10.3389/fdest.2025.1614781

Experimental characterization of electron transport and electroluminescence in xenon-molecular mixtures

C. A. O. Henriques[1]*, L. M. P. Fernandes[1], P. A. O. C. Silva[1], D. González-Díaz[2], C. D. R. Azevedo[3], J. M. F. dos Santos[1] and C. M. B. Monteiro[1]

[1]LIBPhys, LA-REAL, Physics Department, University of Coimbra, Coimbra, Portugal, [2]Instituto Gallego de Física de Altas Energías, Universidade de Santiago de Compostela, Santiago de Compostela, Spain, [3]I3N, Physics Department, University of Aveiro, Aveiro, Portugal

We have developed a comprehensive methodology to measure electron transport and electroluminescence parameters in xenon-based gaseous detectors using photosensor waveform analysis. Our approach integrates measurements of the Fano factor, electroluminescence fluctuations (Q-factor), scintillation probability, electron drift velocity, diffusion, and attachment coefficients into a unified experimental framework, with particular focus on the effects of molecular additives. Using a driftless Gas Proportional Scintillation Counter and advanced event-depth analysis, we achieved an energy resolution of (7.42 $\pm$ 0.02)% FWHM with 5.9-keV X-rays, measured the Fano factor in pure xenon (0.222 $\pm$ 0.004), and characterized the impact of CF_4, CH_4, and CO_2 additives on detector performance. Electron transport measurements showed good agreement with Magboltz simulations, validating our methodology. Through Monte Carlo modeling of electron loss mechanisms, we quantified how attachment affects both electroluminescence yield and statistical fluctuations, enabling separation of attachment effects from other yield-degradation mechanisms for accurate determination of scintillation probabilities. For applications requiring optimal position resolution through reduced diffusion, we compared three molecular additives at concentrations providing equivalent electron cloud spread (2.75 mm after 1 m drift): Xe-CF_4 (0.015%) maintains near-100% scintillation probability but introduces significant electron attachment affecting energy resolution; Xe-CH_4 (0.220%) reduces the scintillation probability by approximately 30% with minimal attachment; while Xe-CO_2 (0.041%) combines reduced scintillation, moderate attachment, and VUV opacity. These findings provide a quantitative foundation for selecting optimal additives based on application-specific priorities in rare-event detection experiments.

KEYWORDS

electroluminescence, electron transport, electron attachment, scintillation probability, xenon electron diffusion, gas proportional scintillation counter, time projection chamber, neutrinoless double beta decay

1 Introduction

Gaseous xenon time projection chambers (TPCs) have become increasingly important for rare-event detection experiments, including searches for neutrinoless double-beta decay, double-electron capture, and directional dark matter (Novella et al., 2023; Yan et al., 2024; Bo et al., 2025; Aprile et al., 2019; Aprile et al., 2025; Nugren et al., 2013; Adams et al., 2021). Compared to liquid xenon (Aprile et al., 2025; Aalbers et al., 2023; Cui et al., 2017; Albert et al., 2018; Gando et al., 2016; Abe et al., 2016), gaseous xenon TPCs offer superior energy resolution and enable topological reconstruction of event signatures, capabilities that have been demonstrated for both double beta decay and double electron capture detection (Luscher et al., 1998; Ferrario et al., 2016; Gavrilyuk et al., 2015). Such topological reconstruction is not viable in liquid xenon, where the extremely compact primary ionization trail prevents pattern-based event discrimination.

Optical TPCs using electroluminescence (EL) amplification have emerged as particularly promising instruments. These detectors can achieve energy resolutions as low as 0.7% FWHM at 2.5 MeV ($Q_{\beta\beta}$ for $\beta\beta0\nu$ decay of ^{136}Xe) (Renner et al., 2019), a 2-4 times improvement over TPCs based on charge avalanche readout (González-Díaz et al., 2015). Additionally, EL readout through photosensors electrically isolates the amplification region, providing greater immunity to electronic noise, radio-frequency pickup, and high-voltage discharges.

Despite their advantages, gaseous xenon TPCs face a significant challenge: large electron diffusion, which degrades the detector's ability to reconstruct event topologies. This diffusion results from inefficient energy loss during elastic collisions between electrons and xenon atoms (Renner et al., 2017). One promising approach to mitigate this problem is the addition of molecular gases (e.g., CO_2, CH_4, or CF_4) to xenon, even at sub-percent concentrations. These molecules introduce vibrational and rotational energy states that provide additional pathways for electron energy transfer through inelastic collisions. As a result, the electron energy distribution in the drift region stabilizes below the first vibrational energy levels (~0.1 eV), approaching the Maxwellian (thermal) limit. Consequently, diffusion is greatly reduced. (Azevedo et al., 2016).

Historically, the addition of molecular species to noble gases was believed to dramatically reduce EL yield (Takahashi et al., 1983). The concern was that electrons would lose energy through collisions with molecular impurities before gaining sufficient energy from the electric field to excite xenon atoms, thus reducing photon production. Additional mechanisms for scintillation loss include excimer quenching, photo-absorption, and electron attachment (Azevedo et al., 2018). However, recent experimental studies with Xe-CO_2, Xe-CH_4, and Xe-CF_4 mixtures have revealed that the degradation in EL yield and associated fluctuations is less severe than previously anticipated (Henriques et al., 2017; Henri et al., 2019).

To optimize xenon-based TPCs with molecular additives, several critical parameters must be carefully measured and balanced. First, as said, electron drift velocity and diffusion directly affect the TPC's position resolution and constitute the primary motivation for molecular gas doping. Equally important is the scintillation probability (SP), defined as the ratio of detectable VUV photons to the number of excited xenon atoms. In pure xenon, this probability exceeds 97% (Azevedo et al., 2018). The SP remains largely independent of the electric field because the dominant atomic states in EL ($1S_4$ and $1S_5$) and their scintillation mechanisms are minimally affected by field variations. Notably, SP is almost independent between primary and secondary scintillation mechanisms because higher energy states typically produced in primary scintillation will rapidly cascade radiatively or collisionally to the low-lying $1S_4$ and $1S_5$ states (Azevedo et al., 2018). This consistency means that SP measurements effectively evaluate an additive's impact on both primary and secondary scintillation yields (Azevedo et al., 2018). Another crucial parameter is the electron attachment coefficient, which quantifies the likelihood of electron capture by neutral molecules per unit distance traveled. Electron attachment not only reduces EL yield by effectively shortening the electron trajectory but, more critically, it introduces statistical fluctuations in the EL gain, significantly degrading the intrinsic energy resolution. The attachment coefficient depends on both electron kinetic energy (thus electric field strength) and the collision probability with impurity molecules. Among common molecular additives at concentrations that provide comparable diffusion reduction, CH_4 most strongly affects scintillation probability, CF_4 exhibits the highest electron attachment, and CO_2 presents moderate attachment with significant impact on scintillation probability (Henriques et al., 2019; Azevedo et al., 2018; Azevedo et al., 2016).

In this research, we present a comprehensive experimental methodology for measuring these fundamental parameters in gaseous xenon doped with molecular additives. Using a driftless Gaseous Proportional Scintillation Counter (dGPSC) and advanced waveform analysis techniques, we extract electron drift velocity, longitudinal electron diffusion, attachment coefficients, intrinsic energy resolution, and scintillation probability directly from electroluminescence signals. We validate our approach through comparison with both theoretical predictions and previous experimental results.

2 Experimental setup

The experimental setup comprises three main subsystems: (1) a gas system equipped with a Residual Gas Analyzer (RGA) for doping xenon with molecular species and measuring their concentrations in real time; (2) a driftless Gaseous Proportional Scintillation Counter (dGPSC) (Henriques et al., 2017; Henriques et al., 2019) for studying electroluminescence and electron drift parameters; and (3) a data acquisition system to record the detector's photosensor waveforms.

2.1 Gas system

An RGA is a highly sensitive mass spectrometer commonly employed for monitoring contamination and detecting leaks in vacuum systems (Mao and Leck, 1987). Its operation is typically limited to a maximum pressure of 10^{-4} mbar. To probe the pressurized dGPSC gas, a heated stainless steel capillary was utilized. The total pressure inside our RGA (RGA 200 from SRS) was maintained below 1×10^{-5} mbar to ensure device linearity, as

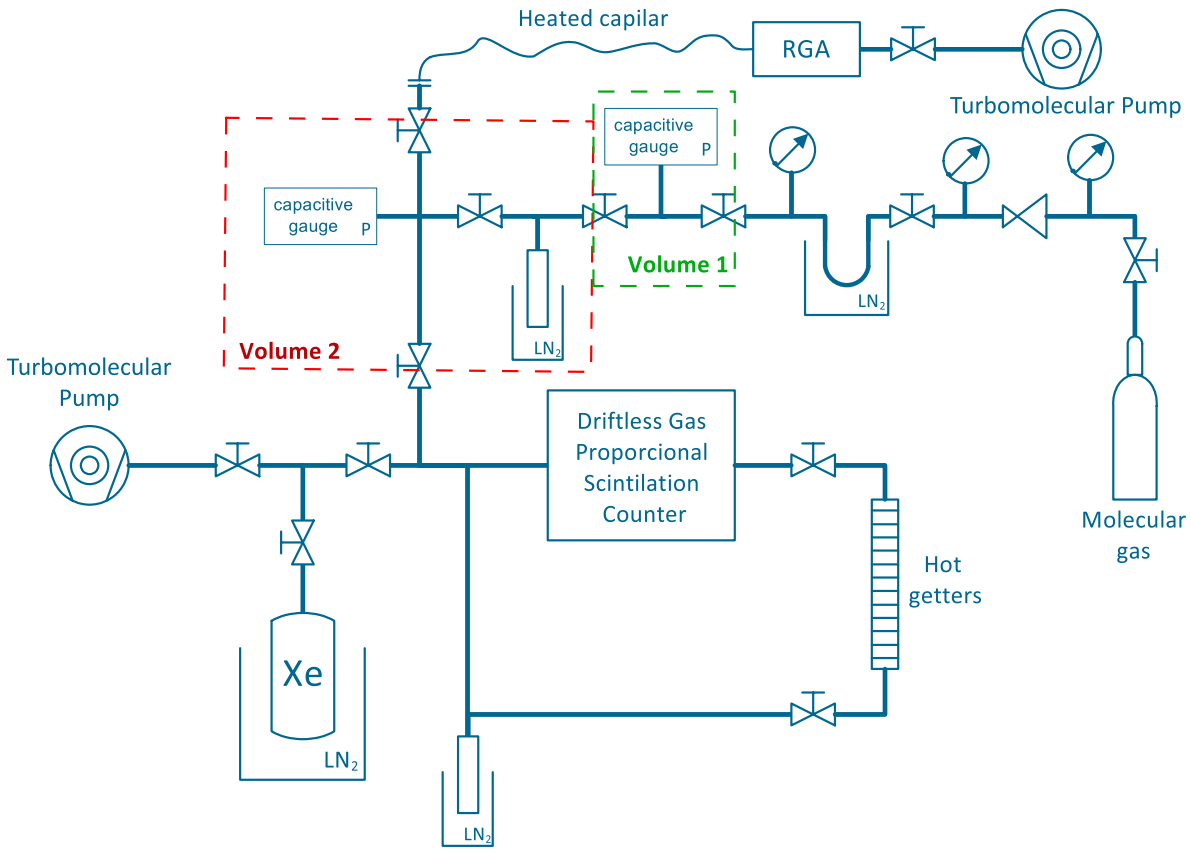

FIGURE 1
Schematic of the gas system used in this work, incorporating the dGPSC, the RGA, and the two calibration volumes.

recommended by the manufacturer. The complete gas system is illustrated in Figure 1 and has been detailed in previous studies (Henriques et al., 2017; Henriques et al., 2019).

Given the low concentrations of molecular gases used in this work (120–660 ppm), the RGA and capillary system require careful calibration for each additive. Calibration mixtures were prepared in two small volumes, each monitored by a capacitive pressure gauge. The concentration of molecular species is determined from the initial pressures of the molecular gas (in volume 1) and xenon (in volume 2), and the final pressure after combining the two volumes, based on the ideal gas law. The final pressure of these mixtures was set to 1.2 bar, consistent with the gas pressure during detector operation, to ensure the reliability of the RGA calibration. The purity of the detector filling gas is continuously maintained by circulation through hot getters (SAES St-707 (SAES, 2025)) in a closed loop by convection. This purification setup was extensively detailed and benchmarked in our previous work (Teixeira et al., 2025). For measurements with pure xenon, the getters are maintained at 250 °C to maximize purity; during electroluminescence measurements with mixtures, the temperature is reduced to approximately 100 °C to minimize additive absorption. Although the getters' performance is not optimal at these lower temperatures, it remains acceptable. A slight reduction in the pure xenon EL yield (up to 7%) was observed compared to that obtained at 250 °C, after several days of operation.

2.2 The driftless GPSC

In contrast to a conventional GPSC (dos Santos et al., 2001), the driftless GPSC lacks a drift region, with radiation absorbed directly within the electroluminescence region (Simons and de Korte, 1989). This distinctive detector geometry is leveraged in this work to measure specific electron drift parameters that would otherwise remain inaccessible.

A simplified schematic of our dGPSC is presented in Figure 2. The 2.5-cm-thick EL region is defined by an aluminized Kapton radiation window (8 mm in diameter) mounted on a stainless-steel holder and by the PMT quartz window, which is vacuum-evaporated with a chromium grid (strips with a width of 100 μm, spacing of 1000 μm, and thickness of 80 nm) electrically connected to the photocathode pin. The PMT (model EMI D676QB, 52 mm in diameter, with a 45-mm effective photocathode diameter, multi-electron rise time of 4 ns, multi-electron FWHM of 6.5 ns, and electron transit time of 40 ns) is epoxied to a cylinder made from ceramic (Macor), which couples to the stainless-steel detector enclosure (approximately 10 cm in diameter) connected to the gas circulation tubing. This PMT model is sensitive to wavelengths ranging from 150 to 650 nm, thus covering the VUV second continuum of Xe electroluminescence (Fujii et al., 2015). The D676QB is a customized eight-dynode version of the 9266QB model, and its quantum efficiency can be found on the

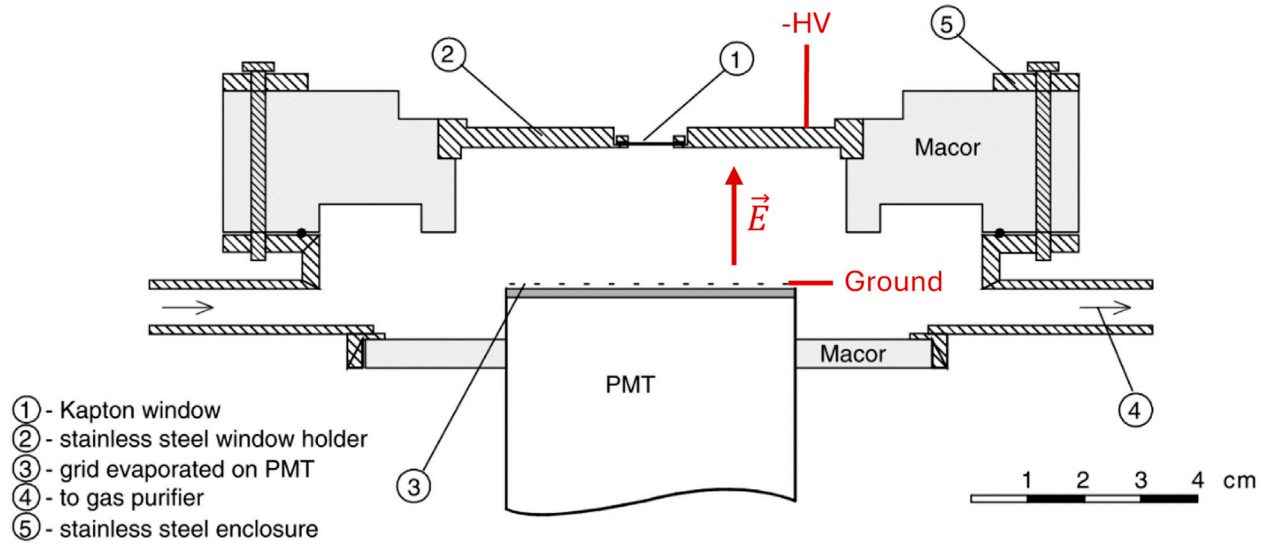

FIGURE 2
Schematic of the driftless GPSC used in this work.

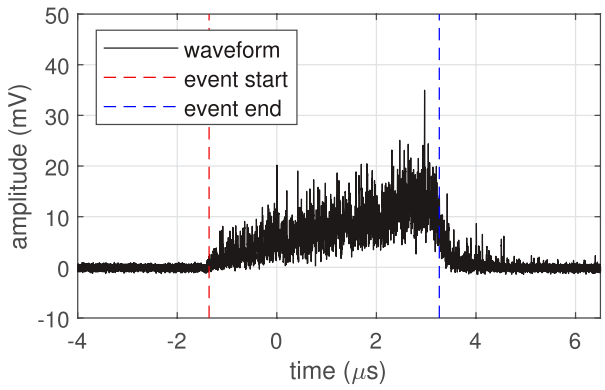

FIGURE 3
Typical PMT waveform obtained by irradiating the dGPSC with 5.9-keV X-rays (before applying the 20-point moving average).

manufacturer's website (Enterprises Limited, 2025). The electric field across the EL region is approximately uniform, with variations of less than 15% as determined from simulations within the studied electric field range (1.5–3.5 kV cm^{-1} bar^{-1}). This dGPSC design has been thoroughly described in previous studies (Simões et al., 2001; Simões et al., 2003).

2.3 Data acquisition system

The photosensor output of a GPSC is typically amplified, shaped, and recorded using a charge-sensitive pre-amplifier, a shaping linear amplifier, and a Multi-Channel Analyzer. However, this data acquisition system fails to preserve the temporal information of the photosensor signal, which is essential for analyzing the dynamics of electron drift and scintillation production. Consequently, the PMT output was directly connected to an oscilloscope (WaveRunner 610Zi from LeCroy) with a sampling rate of 10 GS/s and an analog bandwidth (−3 dB) of 1 GHz, hence avoiding signal distortion introduced by the shaping stages of the pre-amplifier and linear amplifier.

The oscilloscope's 50-Ω DC coupling is employed to match the cable impedance, preventing wave reflections. The PMT bias voltage is set to 1400 V (achiving a gain of ~ 10^5), close to the maximum operating voltage, to enhance the signal-to-noise ratio. Due to memory constraints, the large number of waveforms recorded per run (10^5) are compressed by averaging every 20 consecutive sampled points. While this process reduces high-frequency noise, it lowers the waveform time resolution from 0.1 ns to 2 ns.

Figure 3 displays a typical PMT waveform recorded with 5.9-keV X-rays. The waveform amplitude increases over time as the solid angle subtended by the PMT window grows while the electron cloud (~255 electrons) drifts toward the anode. The EL signal falls abruptly when most electrons are collected at the anode, followed by some afterpulses attributed to PMT aging. Since the initial electron spread is just a few tens of micrometers (Dias et al., 1993), the waveform fall time is primarily governed by longitudinal electron diffusion effects rather than the initial electron cloud size.

A pre-processing algorithm was developed to discriminate background events (e.g., cosmic radiation) and waveforms with characteristics unsuitable for further analysis. This is particularly important for time-dependent measurements. For instance, a waveform containing two events would yield an anomalously long duration measurement. The discrimination algorithm rejects waveforms based on baseline cleanness, event duration, and pulse shape. Additionally, the oscilloscope baseline offset is measured at the start of each recorded waveform and corrected accordingly.

Waveforms were recorded using two different radioactive sources. For most measurements, we employed a ^{55}Fe source, which produces characteristic X-rays at 5.9 keV (Mn K–α line) and 6.4 keV (Mn K–β line). For measurements requiring better statistics at deeper interaction depths, particularly electron drift

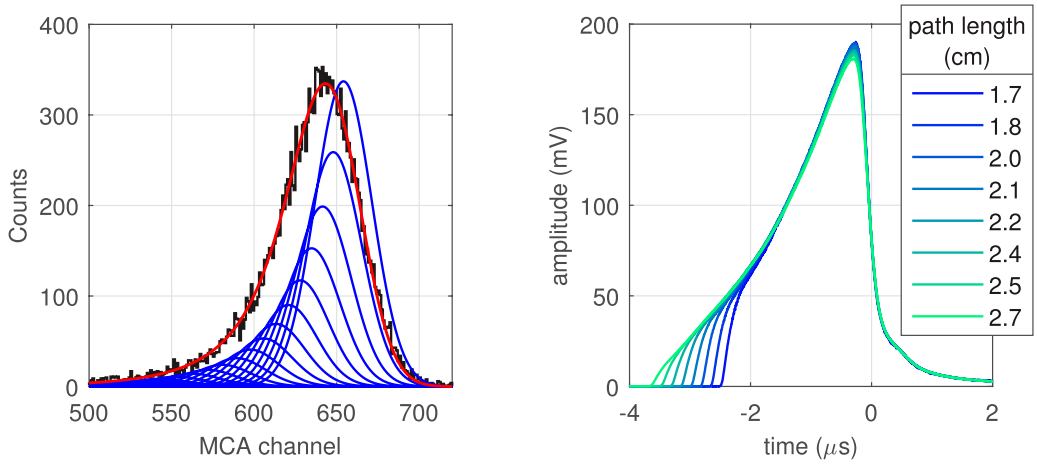

FIGURE 4
Depth-dependent response characteristics of the dGPSC: (Left) Pulse-height distribution acquired with 5.9-keV X-rays (black), showing the asymmetric shape typical of driftless detectors. The theoretical response function (red) is constructed as a superposition of Gaussian components (blue, amplitude scaling arbitrary), each representing interactions at a specific depth. (Right) Experimentally measured waveforms in pure xenon, averaged across events with similar drift path lengths.

velocity and longitudinal diffusion measurements, we used a ^{244}Cm source which provides higher energy X-rays with greater penetration (Pu L–α 14.3 keV, Pu L–β_2 17.3 keV, Pu L–β_1 18.3 keV and Pu L–γ 21.4 keV). In both cases, a 4-mm thick lead collimator with a 2-mm diameter aperture was used to form a narrow X-ray beam. For the ^{55}Fe source, a chromium filter was employed to attenuate the 6.4 keV Mn K$_\beta$ component, resulting in a clean 5.9 keV full absorption peak. For the ^{244}Cm measurements, only events within the 14.3 keV peak were selected for analysis.

3 Methods and results

3.1 X-ray penetration

Unlike conventional GPSCs, the response of a driftless detector exhibits a strong dependence on X-ray interaction depth. Since the number of EL photons is proportional to the electron drift distance, monoenergetic X-rays produce a pulse-height distribution with a characteristic left-sided tail when measured using standard data acquisition systems. As illustrated in Figure 4 (left), this distribution can be decomposed into multiple Gaussian functions, each corresponding to interactions at a specific depth, with amplitudes that follow the exponential X-ray absorption law. In gas mixtures where electron attachment occurs, the distribution may additionally develop a right-sided tail, as deeper events experience less electron loss.

Assuming constant electron drift velocity, the PMT waveform duration is directly proportional the electron drift path length. This relationship enables depth-specific analysis by grouping waveforms according to their duration. Figure 4 (right) shows averaged waveforms for different interaction depths. In pure xenon, where electron loss is negligible, shorter waveforms from deeper interactions maintain amplitude profiles consistent with longer ones from shallower depths. The characteristic shape of these waveforms is primarily determined by geometrical factors, particularly the varying solid angle subtended by the PMT as electrons drift through the anode.

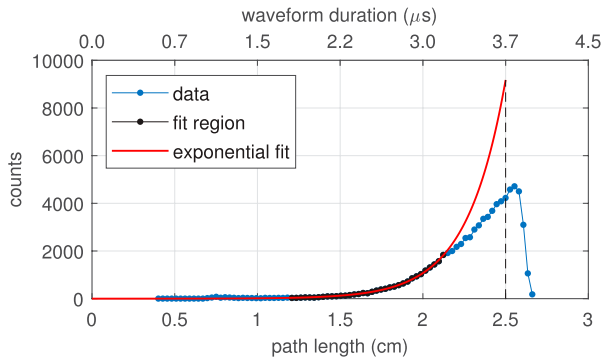

FIGURE 5
Histogram of event durations (blue and black points) and theoretical X-ray attenuation curve (red), used to compute the conversion factor between event duration (upper axis) and corresponding electron drift path length (bottom axis).

3.1.1 Drift path length distribution

The depth distribution of X-ray interactions can be quantitatively analyzed by plotting event frequency as a function of waveform duration. For each event, duration was measured between the 1%-rising edge and the 50%-falling edge thresholds relative to waveform amplitude. Prior to this measurement, a moving average filter was applied to waveforms to reduce high-frequency noise. Using this method, our definition of event duration encompasses the interval from the initiation of the scintillation process to approximately the moment when the electron cloud's centroid reaches the anode. These two limits are also illustrated in Figure 3.

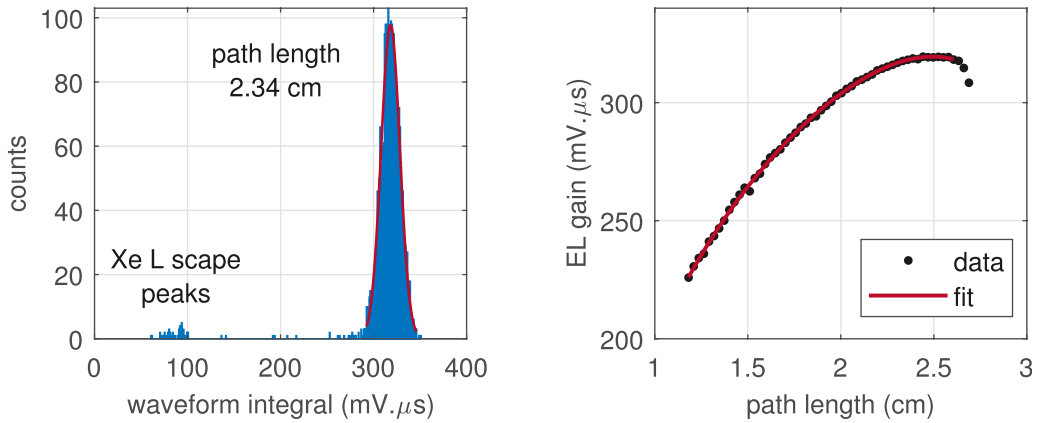

FIGURE 6
Depth-dependent EL gain characterization: (Left) Charge distribution for 5.9-keV X-rays interacting at a path length of approximately 2.34 cm, with the Gaussian fit centroid used to determine the relative EL gain. (Right) Variation of EL gain as a function of electron drift path length, fitted with a fourth-degree polynomial function (excluding the three longest path length data points due to edge effects).

Figure 5 presents an example distribution of event durations obtained with 5.9-keV X-rays. The data exhibit the expected exponential absorption law of X-rays in matter, with notable deviations observed only for longer-duration waveforms (leading to apparent drift path lengths exceeding the detector's physical length of 2.5 cm). These deviations from theoretical predictions are attributed to two primary factors: (1) the weaker electric field near the detector window (12 μm-thick Kapton foil, which bends outward due to differential gas pressure) and (2) statistical fluctuations in the electroluminescence photon burst duration.

To convert event duration into mean electron drift path length, we first fit the event duration distribution with an exponential function over the range of approximately 1.2–2.2 cm, where the data closely follow an exponential trend. We then apply a scaling procedure to determine this conversion factor. Since the maximum physical drift path is 2.5 cm, measured events with apparent path lengths exceeding this limit were actually produced below the 2.5-cm threshold. Accordingly, the conversion factor is scaled such that the excess area (events measured beyond 2.5 cm) equals the deficit area (between the measured and fitted distributions below 2.5 cm). This ensures event count conservation and maps zero duration to zero drift path length (the PMT's transit time spread, ~10 ns, is negligible when compared to electron drift times). The uncertainty in the measured drift path length is estimated to be ~10%.

The X-ray attenuation coefficient extracted from the exponential fit after conversion factor adjustment provides an independent validation of our calibration method. The experimental value (i.e., an attenuation length $\lambda = 0.233 \pm 0.023$ cm) agrees well with theoretical attenuation expected for 5.9-keV X-rays in xenon at a pressure of ~1.2 bar and a temperature of ~305 K ($\lambda = 0.226$ cm), showing only a 10% relative deviation.

With this calibration established, we can classify all PMT waveforms according to their electron drift path length. This classification method was used to create the color-coded waveform representation in Figure 4 (right).

3.1.2 Electroluminescence gain distribution

The PMT charge generated by each X-ray interaction can be obtained by integrating the PMT waveform from 100 ns before the start of the event to 150 ns after the event termination. We present these charge values in the natural units of the integral (mV·μs), since the voltage across the oscilloscope's 50-Ω input resistor is directly proportional to the PMT current. This integration window excludes most PMT afterpulsing, which would otherwise degrade the detector's energy resolution. By analyzing events with similar drift path lengths, we can compute the charge distribution for specific X-ray interaction depths. Figure 6 (left) presents an example charge distribution for interactions occurring at a path length around 2.34 cm.

The centroid of the 5.9-keV full-absorption peak in these distributions is directly proportional to the number of EL photons collected by the PMT for events at the corresponding depth. To characterize the EL gain dependence on interaction depth, we fitted Gaussian functions to the full-absorption peaks of charge distributions obtained at various path lengths. Figure 6 (right) shows the resulting relationship between the EL gain and drift path length, which is well-described by a fourth-degree polynomial function.

This depth-dependent gain variation is primarily governed by geometric factors, specifically the solid angle subtended by the PMT as electrons drift toward it, and remains independent of both X-ray energy and electric field, as confirmed in our experimental measurements (see chapters 5 and 6 in (Henriques, 2019)). The fitted polynomial function is then used to determine the appropriate EL gain correction applied to each waveform charge value, based on its measured drift path length.

3.2 Intrinsic energy resolution

Figure 7 presents the typical dGPSC energy spectrum obtained with 5.9-keV X-rays after applying depth EL gain corrections derived from the polynomial fit shown in Figure 6 (right). The

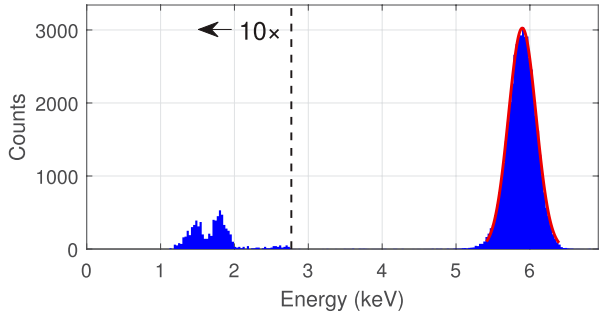

FIGURE 7
Energy spectrum for 5.9-keV X-rays after applying depth-dependent gain corrections, measured at an EL field of 3.2 kV cm^{-1} bar^{-1}. The spectrum shows the main full-absorption peak fitted with a Gaussian function (used to determine the FWHM energy resolution, (7.42 ± 0.02) %) and two smaller L-shell xenon escape peaks on the left (magnified by 10), which were used together with the main peak for energy calibration.

spectrum was calibrated in energy using the 5.9-keV full-absorption peak and the two L-shell xenon escape peaks visible on the left side of the spectrum.

In contrast to the uncorrected energy spectrum obtained with the standard data acquisition system (Figure 4, left), the full-absorption peak now exhibits a symmetrical Gaussian profile. This correction procedure significantly improves the detector's energy resolution from approximately 9%–7.4% FWHM, slightly exceeding the typical performance of standard GPSCs (dos Santos et al., 2001). This enhancement demonstrates the value of utilizing temporal information from the PMT signal to compensate for X-ray penetration effects in the detector response.

Various fluctuation sources contribute to the energy resolution (R_E) of a GPSC, as expressed by Equation 1 (Oliveira et al., 2011):

$$R_E = 2\sqrt{2\ln 2}\sqrt{\frac{F}{\bar{N}_e} + \frac{Q}{\bar{N}_e} + \frac{1}{\bar{N}_{pe}}\left(1 + \frac{\sigma_G^2}{G^2}\right)} \quad (1)$$

The first term under the square root represents the relative fluctuations in the number of ionization electrons produced by the interacting radiation, characterized by the Fano factor ($F = \sigma_e^2/\bar{N}_e$), where $\bar{N}_e$ is the average number of primary electrons and σ_e is the corresponding standard deviation. The second term accounts for relative fluctuations in the number of EL photons generated per primary electron, where $\bar{N}_{EL}$ is the average number of EL photons and $Q = (\sigma_{EL}/\bar{N}_{EL})^2$ is the square of the relative standard deviation. The final term describes relative fluctuations in the photosensor signal, arising from the number of photoelectrons emitted from the PMT photocathode ($\bar{N}_{pe}$), which follows a Poisson distribution, and the relative fluctuations in the electron avalanche gain within the PMT dynodes, with G and σ_G representing the average gain and its standard deviation, respectively. The average number of photoelectrons is given by $\bar{N}_{pe} = k\bar{N}_e\bar{N}_{EL}$, where k is the overall light collection efficiency, influenced by factors such as the anode grid optical transparency, PMT quantum efficiency, and the solid angle subtended by the PMT photocathode.

The intrinsic energy resolution of a detector is defined as the statistical limit imposed by the gas physics, independent of detector geometry or photosensor characteristics, providing a valuable metric for assessing fluctuations in electroluminescence and primary charge production. To isolate the PMT contribution (the final term in Equation 1) from the overall energy resolution, we experimentally measured the dependence of PMT signal fluctuations on $\bar{N}_{pe}$. A blue LED positioned in front of the dGPSC Kapton window was driven by a pulse generator (BNC Model PB-5) with pulse duration, rise time, and fall time adjusted to match typical dGPSC waveforms. The LED intensity range was selected to span the full range of PMT charge values observed with X-rays. As expected, the relative variance in the recorded PMT charge of LED pulses was found to be inversely proportional to $\bar{N}_{pe}$. More information on the PMT characterization can be found in (Henriques, 2019). This relation was then used to estimate the PMT contribution to the energy resolution in X-ray runs.

In pure xenon, relative fluctuations in EL photon production (Q-factor) are significantly smaller than fluctuations in primary charge production (Fano factor) (Oliveira et al., 2011). We therefore neglect the Q-factor term in Equation 1 and use the PMT contribution measured via LED calibration to extract the Fano factor in pure Xe directly from the energy resolution. The number of primary electrons produced by 5.9-keV X-rays can be estimated using the mean energy required to produce an ion-electron pair ($w_i \approx 22$ eV (Dias et al., 1997)) and the X-ray energy (E_x) as $\bar{N}_e = E_x/w_i$. In this way, we determined a Fano factor of 0.222 ± 0.004, which aligns well with experimental values reported in the literature, ranging from 0.12 to 0.26 (do Carmo et al., 2008). The primary uncertainty in the Fano factor stems from the statistical error of the energy resolution measurement, which remains minimal thanks to the large sample size (~ 10^5 waveforms). Nevertheless, this value should be considered an upper limit, since Equation 1 does not account for all fluctuation sources (e.g., depth-dependent variations in photon-burst duration).

Previous determinations of the Fano factor in noble gases have predominantly relied on the infinite light extrapolation technique (do Carmo et al., 2008), which is susceptible to systematic errors arising from the electric field dependence of gas-related fluctuations (Henriques, 2019).[1] Our methodology eliminates this dependence, potentially yielding more accurate results.

The Q-factor encompasses several sources of fluctuations: those arising from the formation and quenching of excited states, and those associated with electron loss mechanisms. In pure xenon, fluctuations from excited state processes are typically negligible compared to the Fano factor. However, in the presence of some molecular additives, such as CF_4 and CO_2, electron attachment can become a significant contributor to the Q-factor. For additives with high electron attachment coefficients, even sub-percent concentrations can cause the Q-factor to become the dominant

1 At higher electric fields, EL gain fluctuations increase due to ionization processes, while at lower fields, electron-ion recombination can also affect these fluctuations. Consequently, the dependence of R_E^2 on $1/N_{pe}$, as determined by varying the electric field, is influenced not only by PMT-related fluctuations but also by field-dependent gas dynamics

term in Equation 1, severely degrading the detector's energy resolution (Henriques et al., 2019). On the other hand, the impact of the low molecular concentrations studied in this work on the Fano factor is expected to be negligible (Escada et al., 2011), allowing us to assume it remains constant across our measurements. Therefore, the Q-factor in mixtures can be determined by subtracting both the Fano factor contribution (as measured in pure xenon) and the PMT contribution (as characterized through our LED measurements) from the total energy resolution (Henriques et al., 2019). For a detailed discussion of energy-resolution contributions in pure xenon and in Xe-molecular mixtures, see Chapters 6 and 9 of Ref. (Henriques, 2019).

3.3 Electron transport parameters

Since the dGPSC lacks a drift region, electron kinetic parameters critical for modeling large TPC experiments, such as electron drift velocity and diffusion, cannot be measured under typical drift electric fields. Nevertheless, a systematic study of these parameters at high electric fields is valuable for validating simulation models. Additionally, other drift parameters, such as electron attachment induced at high electric fields, are essential for understanding the fluctuations introduced by molecular additives in the EL signal.

3.3.1 Electron cloud simulation

The evolution of the electron cloud along the drift path can be described by the hydrodynamic approximation of the Boltzmann equation (Gonzalez-Diaz et al., 2018):

$$\frac{\partial N_e}{\partial t} + v_d \frac{\partial N_e}{\partial z'} - D_T\left(\frac{\partial^2 N_e}{\partial x'^2} + \frac{\partial^2 N_e}{\partial y'^2}\right) - D_L \frac{\partial^2 N_e}{\partial z'^2} + \eta v_d N_e = 0 \quad (2)$$

where N_e is the electron density per unit volume, D_T and D_L are the transverse and longitudinal diffusion coefficients respectively, v_d is the drift velocity, and η is the attachment coefficient. Solving this equation yields:

$$N_e(x', y', z', t) = \frac{e^{-\frac{(x'-x)^2+(y'-y)^2}{4D_T(t-t_0)}}}{(4\pi D_T(t-t_0))} \cdot \frac{e^{-\frac{(z'-z+v_d(t-t_0))^2}{4D_L(t-t_0)}}}{(4\pi D_L(t-t_0))^{1/2}} \cdot \bar{n}_e e^{-\eta v_d (t-t_0)} \quad (3)$$

here, (x', y', z', t) represent the coordinates from the observer's point of view, while (x, y, z, t_0) denote the initial position and time of the ionization cloud containing $\bar{n}_e$ electrons.

By projecting the electron density (N_e in Equation 3) along the z-dimension (the drift direction) and neglecting electron attachment, which is a reasonable approximation for pure xenon, Equation 3 can be simplified into a one-dimensional Gaussian function. The standard deviation of this function is directly proportional to the square root of time ($\sigma = \sqrt{2D_L \Delta t}$), and the centroid is directly proportional to time (centroid = $v_d \Delta t$).

Based on this simplification, we simulated the evolution of a Gaussian-distributed electron cloud along the drift axis to analyze the shape of PMT waveforms. Our simulation incorporated the solid angle subtended by the PMT window and the exponential decay rate of the xenon second continuum, which we assumed to be 100 ns (Henriques et al., 2024). The radial charge distribution of the initial electron cloud was obtained from (Dias et al., 1993).

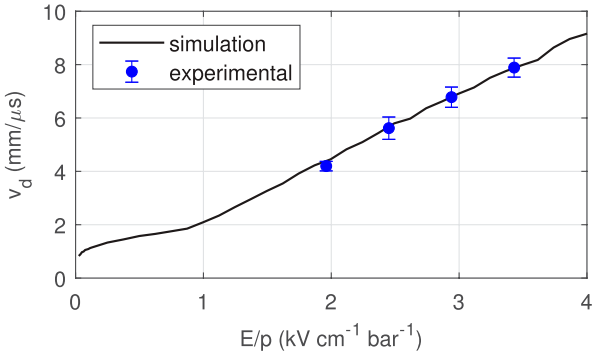

FIGURE 8
Electron drift velocity (v_d) measured with pure xenon at 1.23 bar, plotted against the reduced electric field (E/p). Theoretical values from Magboltz simulation are also depicted.

3.3.2 Electron drift velocity

Section 3.1 introduced a method to determine the conversion factor between the waveform duration and path length drifted by the electron cloud. However, calculating the electron drift velocity (v_d) directly from this factor would overestimate the result due to several broadening effects: the Xe triplet state deexcitation time (~100 ns), the initial spatial distribution of the electron cloud, and longitudinal electron diffusion. Using the electron transport simulation described in Section 3.3.1, we quantitatively assessed these broadening mechanisms and derived appropriate correction factors. Though modest (typically $< 5\%$), these corrections were applied to all v_d measurements.

Figure 8 presents the experimental v_d values measured in pure xenon across various reduced electric fields, alongside expected values from Magboltz simulations (Biagi, 2025; Biagi, 1999). The tight alignment between the two datasets validates our approach.

3.3.3 Longitudinal electron diffusion

To investigate the influence of longitudinal electron diffusion on detector response, we employed the electron cloud simulation detailed in Section 3.3.1. Figure 9 presents a comparison between simulated (left) and experimental (right) PMT waveform trailing edges across various drift path lengths. As shown in simulated waveforms, the effect of longitudinal diffusion is particularly noticeable near the maximum amplitude and in the falling edge. For longer path lengths (red curves), the electron cloud becomes more elongated due to diffusion, resulting in longer fall times and lower waveform maximum amplitudes. Simulation results are closely matched by our experimental observations, confirming that the electron cloud expands longitudinally as it drifts through the EL region. This relationship between waveform fall time and drift path length provides a robust method to quantify the longitudinal electron diffusion coefficient from experimental waveforms.

The majority of afterpulsing in our PMT occurs within the first 900 ns after the emission of the photoelectron. Therefore, the

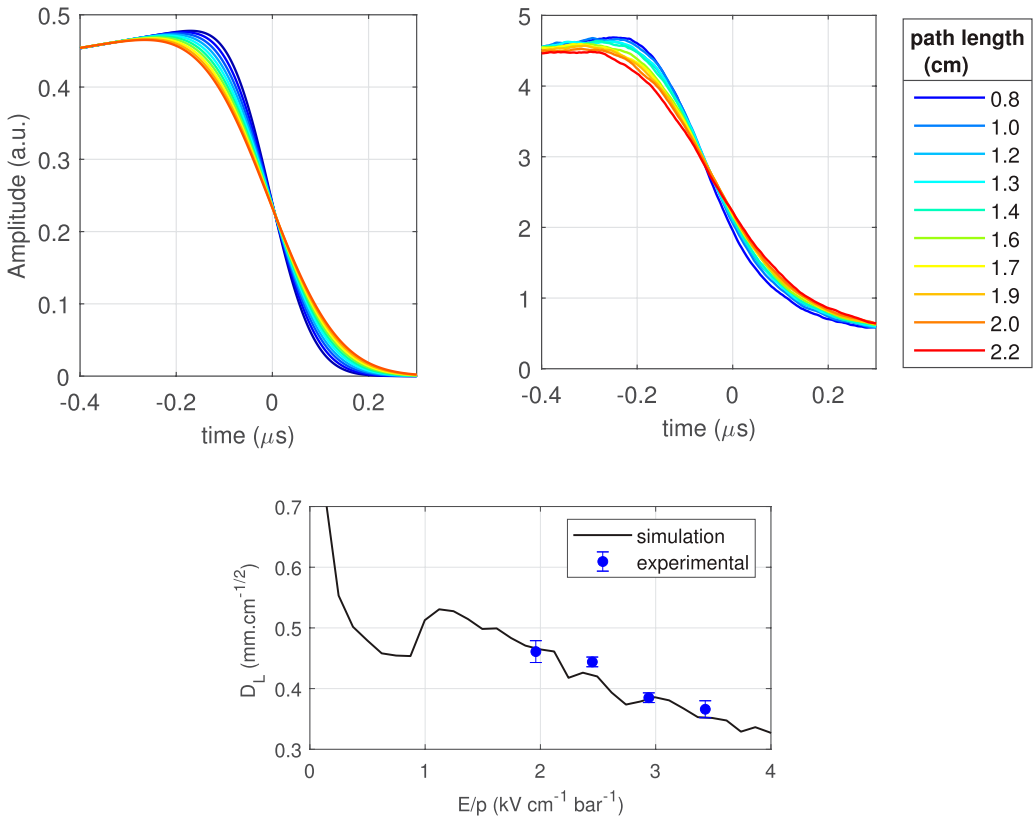

FIGURE 9
Longitudinal electron diffusion: (Top) Simulated (left) and experimental (right) PMT waveform trailing edges for various drift path lengths, showing longer fall times with increasing path length due to diffusion. (Bottom) Measured diffusion coefficient ($D_L^* = \sqrt{2D_L/v_d}$) in pure xenon at 1.23 bar versus reduced electric field, with experimental values compared to Magboltz simulations.

afterpulsing effect on waveform trailing edges remains constant across different drift path lengths, provided waveforms are not shorter than 900 ns. Consequently, while the absolute fall time values are influenced by both afterpulsing and the initial electron cloud spread, only longitudinal diffusion determines how fall time varies with drift path length. As an additional precaution, we restricted our fall time measurements to the region between 90% and 60% of the waveform maximum amplitude, further reducing any residual afterpulsing contributions.

Using our electron cloud simulation framework (Section 3.3.1), we constructed a model that predicts waveform fall times as a function of drift path length. The model incorporates three key parameters: electron drift velocity, longitudinal diffusion coefficient, and the initial spatial spread of the electron cloud. To extract the diffusion coefficient from experimental data, we fitted this model to the measured fall times across various drift path lengths. To minimize the impact of high-frequency noise, average waveforms were used instead of individual waveforms in the fall time measurements. In this fitting procedure, we fixed the drift velocity to our experimentally determined values (Section 3.3.2) while allowing both the diffusion coefficient and initial electron cloud spread to vary as free parameters. To avoid the boundary effects, we excluded data points with path lengths exceeding 1.7 cm from our analysis.

The results of our longitudinal diffusion coefficient measurements are summarized in Figure 9 (bottom), which displays the parameter $D_L^* = \sqrt{2D_L/v_d}$ (representing the spatial spread per unit square root of drift length) for pure xenon at 1.23 bar. Experimental data show reasonable agreement with theoretical predictions from Magboltz simulations (black curve), further validating our waveform-based measurement approach.

3.3.4 Electron attachment

Electron attachment can be quantified by examining average PMT waveforms at different interaction depths, since the number of emitted EL photons is directly proportional to the surviving electron population. Figure 10 illustrates this effect by comparing waveforms from pure Xe and Xe-CF_4 mixtures. Pure xenon waveforms maintain consistent amplitude profiles regardless of interaction depth, indicating negligible electron loss. In contrast, Xe-CF_4 mixtures exhibit a progressive amplitude reduction with increasing drift path length, a clear signature of CF_4-induced dissociative attachment capturing electrons during their drift.

To determine electron attachment coefficients, we developed a method based on the EL signal analysis at a fixed reference position. For each average waveform, we integrated the signal when the electron cloud was between 6.5 and 7.5 mm from the anode. This integration measures the reduced EL yield (Y/p (7 mm)) at this reference position. The shaded green region in Figure 10 (top left) denotes the 6.5–7.5 mm

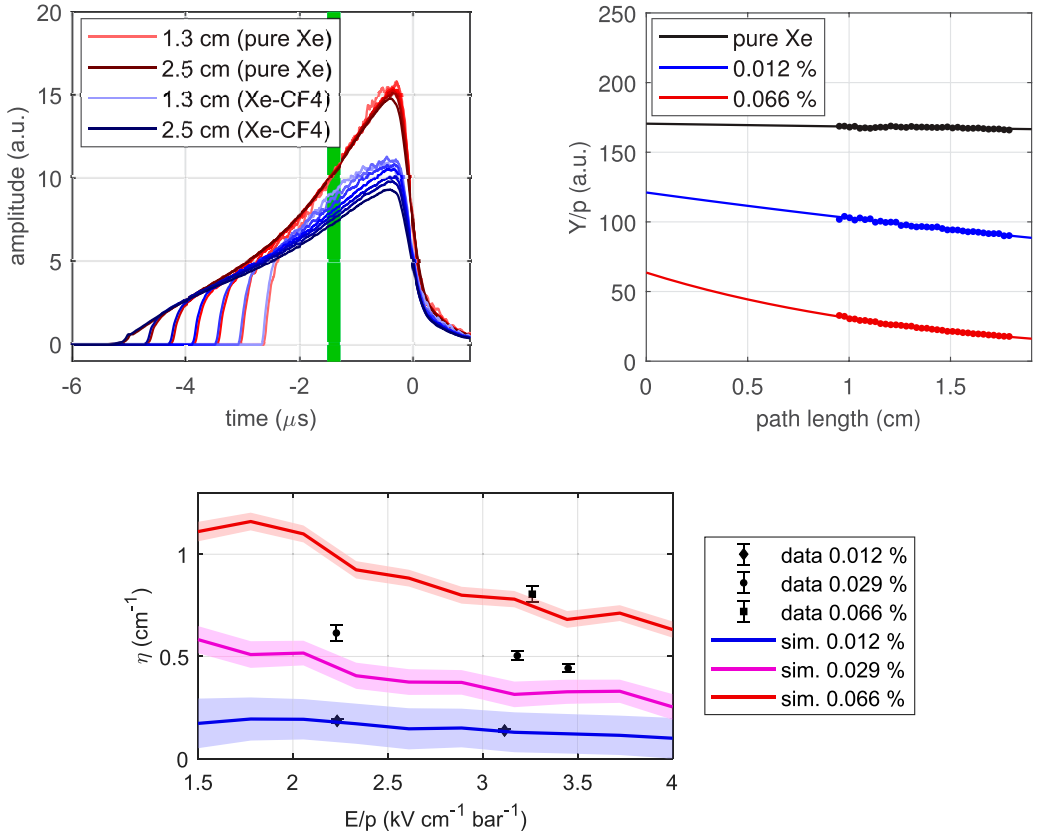

FIGURE 10
Electron attachment characterization: (Top left) Averaged waveforms from pure xenon and 0.012% CF_4 mixture, with CF_4 waveforms normalized to match pure xenon at their initial segments. The green region indicates the integration window used for attachment measurements. (Top right) Reduced EL yield (Y/p (7 mm)) as a function of drift path length (Δx) for pure xenon (2.45 kV cm^{-1} bar^{-1}) and Xe-CF_4 mixtures (0.012% and 0.029% at 2.23 kV cm^{-1} bar^{-1}). Circles represent experimental data, with solid lines showing exponential fits. (Bottom) Attachment coefficients (η) measured for three CF_4 concentrations across various reduced electric fields, compared with Magboltz simulation predictions (shaded bands represent uncertainty).

integration window, whose bounds were determined from the waveform-duration to mean drift-path calibration (Section 3.1.1). By plotting these yield values against the path length (Δx) traveled by electrons before reaching this position (Figure 10 top right), we observe the expected exponential decay curve. The decay constant from exponential fit provides the attachment coefficient (η), which increases with CF_4 concentration while remaining effectively zero for pure xenon.

Figure 10 (bottom) shows the experimental attachment coefficients obtained with three Xe-CF_4 mixtures across several reduced electric fields, alongside theoretical values from Magboltz simulations. There is general good agreement between simulations and experimental data, except for 0.029% CF_4. For this particular concentration, measurements were performed approximately 1 month after the initial detector filling, suggesting possible contamination with additional electronegative species (particularly O_2, H_2O, or CO_2) that may have accumulated over time despite the continuous gas purification.

3.4 Electroluminescence parameters

The temporal information encoded in PMT waveforms enables precise measurement of several key electroluminescence parameters. Through analysis of waveforms produced under different drift distances and electric fields, we can quantify fundamental properties including the scintillation probability, EL yield, statistical fluctuations in the EL process, and the impact of electron attachment on detector performance.

3.4.1 Electron attachment impact on electroluminescence

When evaluating how electron attachment affects EL yield, we must first account for other molecular additive effects that simultaneously influence the signal. Processes such as quenching of atomic and dimer excited states and electron cooling also contribute to EL yield degradation. To isolate the effect of these other processes, we applied the method described in Section 3.3.4, where the EL yield at zero drift path length ($\Delta x \to 0$), before attachment occurs, is given by parameter a in the exponential fit function $f(x) = ae^{-\eta \Delta x}$.

The ratio between a-values for Xe-CF_4 mixtures and pure Xe can be used to rescale the mixture waveforms to effectively remove non-attachment-related degradation effects. This normalization, visible in Figure 10 (top left), allows direct observation and quantification of yield reduction specifically caused by electron attachment.

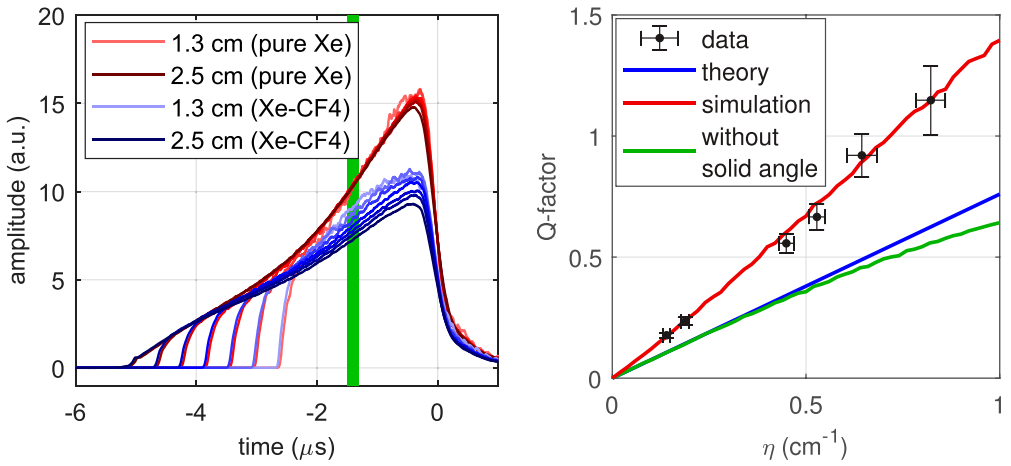

FIGURE 11
Experimental Y_{att}/Y_0 (left) and Q (right) values obtained for various Xe-CF_4 mixtures at different electric fields plotted against their corresponding experimental η-values. The theoretical Y_{att}/Y_0 and Q dependencies on η are also depicted, including simulation results (with and without solid angle considerations) and the linear approximation for small attachment (blue line).

Figure 11 presents our key experimental results quantifying electron attachment effects on electroluminescence, obtained with 5.9-keV X-rays for pure Xe and various Xe-CF_4 mixtures at different electric fields. The left panel presents the relative EL yield under electron attachment conditions (Y_{att}/Y_0) plotted against the corresponding electron attachment coefficients (η). These yield ratios were obtained by integrating rescaled Xe-CF_4 waveforms (with attachment) and comparing them to integrated pure Xe waveforms (without attachment), with η values determined as described in Section 3.3.4. The right panel shows the experimental Q-factors plotted as a function of η. These Q-factors, quantifying statistical fluctuations in the EL process, were measured using the methodology detailed in Section 3.2.

For small attachment values, analytical theory predicts $Q = \eta g/3$ and $Y_{att}/Y_0 = 1 - \eta g/2$ (derived in Ref. (Azevedo et al., 2018)), where g represents the EL region length. However, our data show significant deviations from these approximations, particularly at higher attachment coefficients, as demonstrated in Figure 11. To understand these deviations, we developed a Monte Carlo simulation of the electron drift and attachment process.

The simulation follows individual electrons through the EL region, where each electron's attachment position is generated according to an exponential probability distribution governed by the attachment coefficient. We integrate the photon yield along each electron's trajectory, weighted by the solid angle subtended by the PMT from each position, until either attachment occurs or the electron reaches the anode. The simulation outputs both the mean detected photon yield and its statistical distribution, enabling direct calculation of Y_{att}/Y_0 and Q-factor.

Our simulation results (also shown in Figure 11) demonstrate excellent agreement with experimental data, validating our understanding of the underlying physical processes. Importantly, the simulation revealed that detector geometry significantly influences attachment effects. The sharply increasing solid angle as electrons approach the PMT causes the Q-factor (Equation 1) to degrade approximately twice as much as it would be expected in a constant-solid-angle configuration when attachment coefficients exceed 0.1 cm^{-1}. This degradation stems from increased variability in the number of detected photons when electrons are attached at different positions. While less pronounced than its effect on the Q-factor, the solid angle variation also degrades the Y_{att}/Y_0 value. This geometric effect explains the observed deviations from analytical predictions and highlights an important consideration for optimal detector design.

3.4.2 Scintillation probability

The electroluminescence yield in noble gases exhibits an approximately linear relationship with the reduced electric field, expressed as $Y/p = a(E/p - E_{th}/p)$ (Henriques et al., 2024; Monteiro et al., 2007; Oliveira C. A. B. et al., 2011), a behavior that seems to persist even in the presence of molecular additives (Henriques et al., 2019). In this relation, the EL amplification parameter a directly correlates with the scintillation probability (SP), while the x-intercept parameter E_{th}/p reflects the EL threshold required to initiate electroluminescence.

Molecular additives influence this relationship through three distinct mechanisms: (1) electron cooling, which primarily affects the E_{th}/p value by shifting yield curves toward higher fields; (2) quenching of xenon excited states, which reduces the SP and consequently the a-parameter; and (3) electron attachment, which, due to its characteristic dependence on electric field strength, can also modify the $Y/p(E/p)$ slope or even slightly degrade its linearity. Additional electroluminescence production processes such as Neutral Bremsstrahlung are not considered here as they are negligible compared to excimer-based electroluminescence within our working conditions (Henriques et al., 2022). Therefore, to accurately determine the intrinsic SP, we must first compensate the yield curves for attachment effects using Y_{att}/Y_0 values derived from the Monte Carlo simulation described in Section 3.3.4, given known attachment coefficients.

Figure 12 presents both raw and attachment-compensated EL yield curves for two Xe-CF_4 mixtures (0.012% and 0.029% by

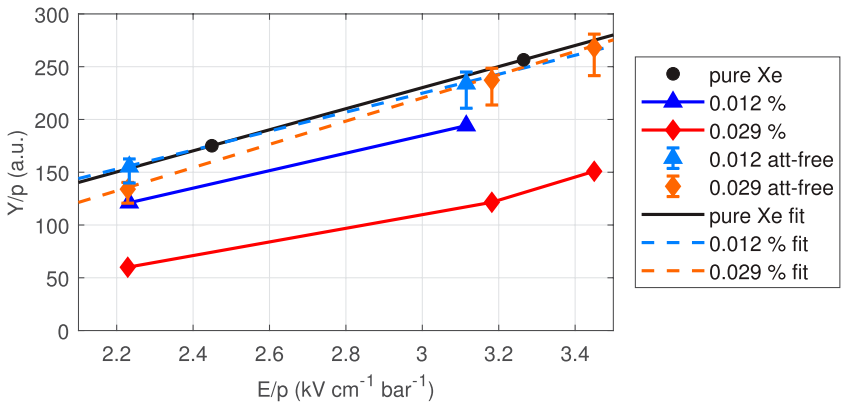

FIGURE 12
Raw and attachment-free EL yield curves for two Xe-CF_4 mixtures (0.012% and 0.029%) alongside pure Xe results, all plotted against the reduced electric field. Linear fits performed to pure Xe and attachment-free mixture data are also shown.

concentration) alongside pure Xe results, plotted against the reduced electric field. After correcting for attachment effects, the mixture yields recover to nearly pure Xe levels, indicating minimal degradation in both SP and EL threshold.

Linear regression analysis (also depicted in Figure 12) of these corrected yield curves resulted in E_{th}/p values of 0.69 ± 0.04 kV cm^{-1} bar^{-1} for pure xenon, compared to 0.57 ± 0.55 and 1.02 ± 0.40 kV cm^{-1} bar^{-1} for the 0.012% and 0.029% CF_4 mixtures, respectively. From the ratio between the slope parameters (a) of corrected mixture yield curves and that of pure Xe (assuming a SP of 100% for pure xenon), we calculated scintillation probabilities of (93 ± 18)% and (112 ± 13)% for the 0.012% and 0.029% CF_4 mixtures, respectively. These results support theoretical predictions that CF_4 at these sub-percent concentrations has negligible impact on SP (Azevedo et al., 2018). Although our data follow expected behavior, the pronounced uncertainties arising from both the small number of field points and the larger CF_4 attachment-correction errors (versus pure xenon) hinder more definitive interpretations of subtle effects.

3.4.3 Scintillation probabilities from historical data

Prior to developing the waveform-based methodology described in this paper, we conducted extensive studies on the effects of molecular additives (CO_2, CH_4, and CF_4) on xenon electroluminescence (Henriques et al., 2017; Henriques et al., 2019). Those earlier investigations employed conventional signal shaping instrumentation that did not preserve temporal waveform information. While such data cannot directly yield parameters like electron drift velocity or longitudinal diffusion, a reasonable estimation of attachment coefficients can be obtained through careful analysis of the recorded pulse-height distributions.

As illustrated in Figure 4 (left), the detector pulse-height distribution can be parameterized by a sum of Gaussian functions, each corresponding to a particular X-ray interaction depth. Electron attachment affects both the EL yield and Q-factor (Figure 11), causing distinctive distortions in the shape of the pulse-height distribution. These attachment-induced changes to the centroids (Figure 6) and sigma values of the Gaussian components can be accessed through the simulation framework described in Section 3.4.1. Using this approach, we can construct a fit function with the attachment coefficient being left as a free parameter. By fitting this model to the experimental pulse-height distributions, the EL yield, energy resolution and attachment coefficient can be obtained. A more detailed description of this methodology can be found in (Henriques, 2019; Henriques et al., 2019).

Using these roughly estimated attachment coefficients, we applied appropriate corrections to the previously measured EL yield curves using the simulated relationship between Y_{att}/Y_0 and η established in Figure 11 (left). The corrected yield curves then allowed determination of scintillation probabilities using the methodology described in Section 3.4.2. Figure 13 presents the results of this re-analysis alongside theoretical predictions from the microscopic simulation framework described in (Azevedo et al., 2018). The concentration uncertainty stems from the Residual Gas Analyzer measurements, whose methodology was extensively detailed in (Henriques, 2019). In Xe-CF_4 and Xe-CO_2 mixtures, the attachment coefficient measurement is the main contribution for SP uncertainty, resulting in larger error bars.

The uncertainty analysis reveals that for CF_4 mixtures, where electron attachment is substantial, the error in the derived attachment coefficient dominates the uncertainty budget for scintillation probability. The concentration uncertainty stems from the Residual Gas Analyzer measurements, whose methodology was extensively detailed in (Henriques, 2019).

The results confirm our theoretical expectations: quenching of excited xenon states is substantial in both CO_2 and CH_4 mixtures but minimal or absent in CF_4 mixtures. While simulation predictions generally match experimental findings within uncertainty bounds, we observe that the model tends to underestimate scintillation probabilities in low-concentration CH_4 mixtures, suggesting potential refinements to the simulation framework may be necessary. These results align well with our current measurements presented in Section 3.4.2, which are also included in Figure 13 for direct comparison. Although the scintillation probabilities determined in Section 3.4.2 benefit from more precise attachment coefficient measurements, it is ultimately limited by low statistics in the EL yield data points, resulting in comparable error margins in the final scintillation probability values.

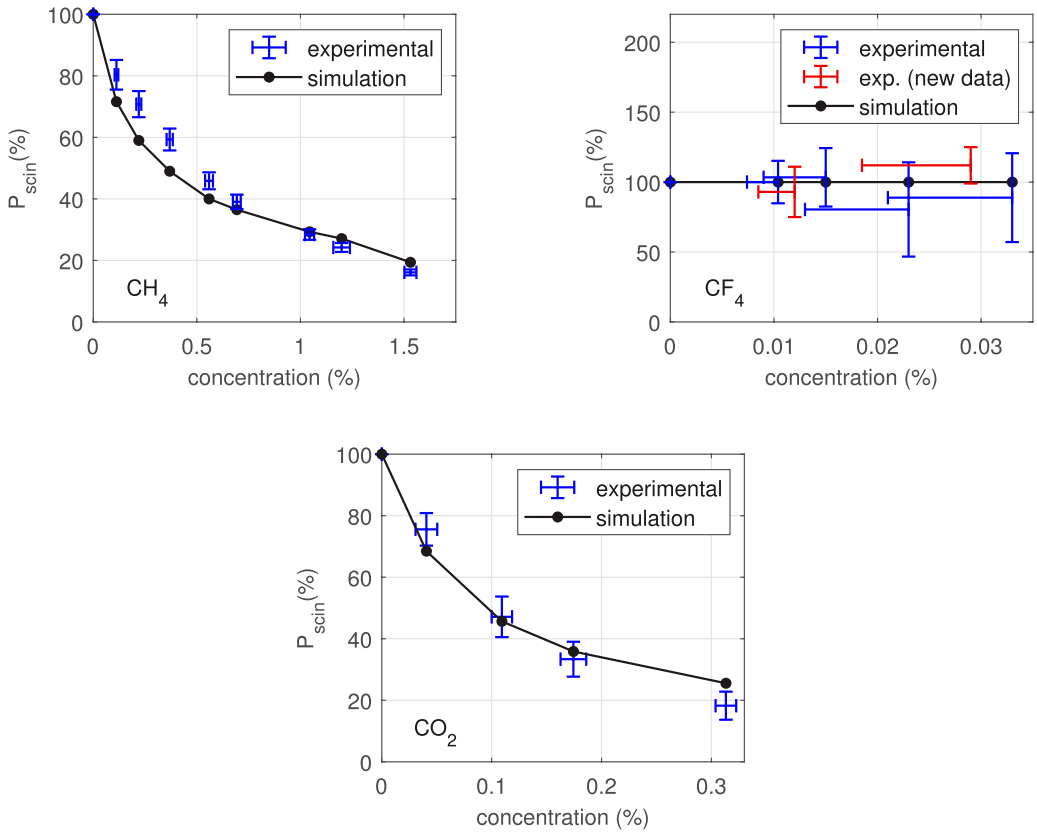

FIGURE 13
Scintillation probabilities obtained from the reanalysis of previous experimental data: Xe-CH_4 at 1.25 bar (top left), Xe-CF_4 at 1.24 bar (top right), and Xe-CO_2 at 1.13 bar (bottom) as a function of molecular additive concentration. Experimental values are compared to theoretical predictions from microscopic simulations. New data corresponding to CF_4 concentrations studied in this work are also included (red data points).

4 Conclusion

This work establishes a comprehensive experimental framework to measure electron transport and electroluminescence parameters in xenon and xenon-molecular mixtures using photosensor waveform analysis. This approach provides detailed understanding of the impact of molecular additives on noble gas detector performance, enabling position resolution optimizations in various applications.

We extensively studied the driftless Gas Proportional Scintillation Counter response, including X-ray penetration effects. This allowed energy spectrum reconstruction using temporal waveform information, achieving an exceptional energy resolution of (7.42 ± 0.02)% FWHM with 5.9-keV X-rays that rivals even the best conventional GPSC performance. Careful characterization of photosensor-related fluctuations enabled direct computation of the intrinsic energy resolution, avoiding the problematic infinite light extrapolation method used in previous studies. This approach allowed us to isolate the Fano factor contribution in pure xenon (0.222 ± 0.004) and to quantify the electroluminescence fluctuations (Q-factors) in Xe-CF_4 mixtures.

Electron drift velocity and longitudinal electron diffusion were measured in pure xenon across various electric fields. The excellent agreement between our experimental results and state-of-the-art simulation predictions validates our measurement methodology. This approach establishes a foundation for future investigations of how molecular additives affect these transport parameters, which are crucial for improving TPCs position resolution.

We developed a precise method to measure electron attachment coefficients by exploiting the X-ray penetration effect characteristic of dGPSC detectors. By analyzing waveforms from various interaction depths in Xe-CF_4 mixtures, we quantified attachment coefficients that showed good agreement with microscopic simulation results. To understand attachment's impact on both EL yield and Q-factor, we implemented a Monte Carlo simulation of electron drift and attachment processes. The simulation results showed remarkable agreement with our experimental measurements, validating our predictive model. A key finding from our analysis is that the variation of the solid angle along the electron drift path, significantly enhances attachment-induced degradation, with the Q-factor approximately doubling compared to predictions in a constant-solid-angle configuration. This finding underscores the importance of the detector geometry when designing future systems for operation with attachment-inducing additives.

Finally, we developed a method to isolate electron attachment effects from other processes degrading electroluminescence yield, including the electron cooling effect. This approach enabled measurement of the scintillation probability in Xe-CF_4 mixtures. We extended this methodology to reanalyze previously published data on EL yield in Xe-CO_2, Xe-CH_4, and Xe-CF_4 mixtures. Although these earlier studies lacked temporal waveform information, we extracted

approximate attachment coefficients by analyzing the characteristic distortions in pulse-height distributions. Combined with our Monte Carlo model predictions of how attachment affects EL yield, these coefficients enabled reliable determination of scintillation probabilities across various molecular additive concentrations.

The EL performance of these molecular species can be compared considering the concentrations required to achieve equivalent diffusion reduction (a 3-dimensional electron spread of 2.75 mm after 1 m drift): CF_4 (0.015%), CH_4 (0.220%), and CO_2 (0.041%) (Henriques et al., 2019). Our analysis revealed distinct trade-offs among these additives. While CF_4 preserves almost 100% of xenon's scintillation probability, it introduces significant electron attachment that degrades the Q-factor and consequently the energy resolution (Henriques et al., 2019). Nevertheless, CF_4 remains attractive for applications prioritizing light yield over energy resolution, particularly in systems with low photon collection efficiency where Q-factor contributions are less significant. CH_4 reduces scintillation probability by approximately 30% but causes minimal electron attachment, making it suitable for applications where energy resolution is critical and sufficient photons are collected to compensate for reduced light yield. CO_2 combines the disadvantages of both alternatives, reducing scintillation probability by 30%, introducing moderate attachment effects, and exhibiting opacity to VUV light (Henriques et al., 2019), making it generally the least suitable option.

Our results provide a comprehensive understanding of the impact of molecular additives on noble gas detector performance, offering valuable insights for future detector design and optimization. The experimental framework developed in this work can be readily applied to other gas-based detectors, enabling detailed studies of electron transport and electroluminescence properties in a wide range of experimental conditions.

Data availability statement

The datasets presented in this article are not readily available because it is confidential. Requests to access the datasets should be directed to henriques@uc.pt.

Author contributions

CH: Data curation, Funding acquisition, Validation, Resources, Conceptualization, Visualization, Project administration, Investigation, Supervision, Writing – review and editing, Methodology, Writing – original draft, Formal Analysis, Software. LF: Supervision, Writing – review and editing. PS: Software, Writing – review and editing. DG-D: Methodology, Writing – review and editing, Software. CA: Software, Writing – review and editing. JS: Project administration, Writing – review and editing. CM: Supervision, Writing – review and editing.

Funding

The author(s) declare that financial support was received for the research and/or publication of this article. This work is supported by FCT, I.P, Lisbon, through projects 2023.13742.PEX, PTDC/FIS-NUC/3933/2021, UIDB/FIS/04559/2020 (LIBPhys) and UIDP/FIS/04559/2020 (LIBPhys), funded through FCT by national funds and PRR, measure RE-C06-i06.m02.

Conflict of interest

The authors declare that the research was conducted in the absence of any commercial or financial relationships that could be construed as a potential conflict of interest.

The author(s) declared that they were an editorial board member of Frontiers, at the time of submission. This had no impact on the peer review process and the final decision.

Generative AI statement

The author(s) declare that no Generative AI was used in the creation of this manuscript.

Publisher's note

References

Aalbers, J., Akerib, D., Akerlof, C., Al Musalhi, A., Alder, F., Alqahtani, A., et al. (2023). First dark matter search results from the LUX-ZEPLIN (LZ) experiment. *Phys. Rev. Lett.* 131, 041002. doi:10.1103/PhysRevLett.131.041002

Abe, K., Hiraide, K., Ichimura, K., Kishimoto, Y., Kobayashi, K., Kobayashi, M., et al. (2016). Search for two-neutrino double electron capture on ^{124}Xe with the XMASS-I detector. *Phys. Lett. B* 759, 64–68. doi:10.1016/j.physletb.2016.05.039

Adams, C., Álvarez, V., Arazi, L., Arnquist, I. J., Azevedo, C. D. R., Bailey, K., et al. (2021). Sensitivity of a tonne-scale NEXT detector for neutrinoless double beta decay searches. *J. High Energy Phys.* 2021, 164. doi:10.1007/JHEP08(2021)164

Albert, J. , Anton, G., Badhrees, I., Barbeau, P., Bayerlein, R., Beck, D., et al. (2018). Search for neutrinoless double-beta decay with the upgraded EXO-200 detector. *Phys. Rev. Lett.* 120, 072701. doi:10.1103/PhysRevLett.120.072701

Aprile, E., Aalbers, J., Abe, K., Ahmed Maouloud, S., Althueser, L., Andrieu, B., et al. (2025). First search for light dark matter in the neutrino fog with XENONnT. *Phys. Rev. Lett.* 134, 111802. doi:10.1103/PhysRevLett.134.111802

Aprile, E., Aalbers, J., Agostini, F., Alfonsi, M., Althueser, L., Amaro, F. D., et al. (2019). Observation of two-neutrino double electron capture in ^{124}Xe with XENON1T. *Nature* 568, 532–535. doi:10.1038/s41586-019-1124-4

Azevedo, C. D. R., Fernandes, L. M. P., Freitas, E. D. C., Gonzalez-Diaz, D., Monrabal, F., Monteiro, C. M. B., et al. (2016). An homeopathic cure to pure xenon large diffusion. *JINST* 11, C02007. doi:10.1088/1748-0221/11/02/C02007

Azevedo, C. D. R., González-Díaz, D., Biagi, S., Oliveira, C., Henriques, C., Escada, J., et al. (2018). Microscopic simulation of xenon-based optical TPCs in the presence of molecular additives. *Nucl. Instrum. Methods Phys. Res. Sect. A Accel. Spectrom. Detect. Assoc. Equip.* 877, 157–172. doi:10.1016/j.nima.2017.08.049

Biagi, S. (2025). Magboltz – transport of electrons in gas mixtures. Available online at: https://magboltz.web.cern.ch/magboltz (Accessed March 12, 2025).

Biagi, S. F. (1999). Monte carlo simulation of electron drift and diffusion in counting gases under the influence of electric and magnetic fields. *Nucl. Instrum. Methods Phys. Res. Sect. A Accel. Spectrom. Detect. Assoc. Equip.* 421, 234–240. doi:10.1016/S0168-9002(98)01233-9

Bo, Z., Chen, W., Chen, X., Chen, Y., Cheng, Z., Cui, X., et al. (2025). Dark matter search results from 1.54 tonne·year exposure of PandaX-4T. *Phys. Rev. Lett.* 134, 011805. doi:10.1103/PhysRevLett.134.011805

Cui, X., Abdukerim, A., Chen, W., Chen, X., Chen, Y., Dong, B., et al. (2017). Dark matter results from 54-Ton-Day exposure of PandaX-II experiment. *Phys. Rev. Lett.* 119, 181302. doi:10.1103/PhysRevLett.119.181302

Dias, T., Dos Santos, J., Rachinhas, P., Santos, F., Conde, C., and Stauffer, A. (1997). Full-energy absorption of X-ray energies near the Xe L- and K-photoionization thresholds in xenon gas detectors: simulation and experimental results. *J. Appl. Phys.* 82, 2742–2753. doi:10.1063/1.366105

Dias, T., Santos, F., Stauffer, A., and Conde, C. (1993). Monte carlo simulation of X-ray absorption and electron drift in gaseous xenon. *Phys. Rev. A* 48, 2887–2902. doi:10.1103/physreva.48.2887

do Carmo, S. J., Borges, F. I., Vinagre, F. L., and Conde, C. A. (2008). Experimental study of the *w*-values and fano factors of gaseous xenon and Ar–Xe mixtures for X-rays. *IEEE Trans. Nucl. Sci.* 55, 2637–2642. doi:10.1109/tns.2008.2003075

dos Santos, J. M. F., Lopes, J. A. M., Veloso, J., Simões, P. C. P. S., Dias, T., Santos, F., et al. (2001). Development of portable gas proportional scintillation counters for X-ray spectrometry. *X-Ray Spectrom.* 30, 373–381. doi:10.1002/xrs.510

Enterprises Limited (2025). *Official website*. Available online at: https://et-enterprises.com/images/data_sheets/9266B.pdf (Accessed June 30, 2025).

Escada, J., Dias, T., Santos, F., Rachinhas, P., Conde, C., and Stauffer, A. (2011). A monte carlo study of the fluctuations in Xe electroluminescence yield: pure Xe vs Xe doped with CH_4 or CF_4 and planar vs cylindrical geometries. *J. Instrum.* 6, P08006. doi:10.1088/1748-0221/6/08/p08006

Ferrario, P., Laing, A., López-March, N., Gómez-Cadenas, J. J., Álvarez, V., Azevedo, C. D. R., et al. (2016). First proof of topological signature in the high pressure xenon gas TPC with electroluminescence amplification for the NEXT experiment. *J. High Energy Phys.* 2016, 104. doi:10.1007/JHEP01(2016)104

Fujii, K., Endo, Y., Torigoe, Y., Nakamura, S., Haruyama, T., Kasami, K., et al. (2015). High-accuracy measurement of the emission spectrum of liquid xenon in the vacuum ultraviolet region. *Nucl. Instrum. Methods Phys. Res. Sect. A Accel. Spectrom. Detect. Assoc. Equip.* 795, 293–297. doi:10.1016/j.nima.2015.05.065

Gando, A., Gando, Y., Hachiya, T., Hayashi, A., Hayashida, S., Ikeda, H., et al. (2016). Search for majorana neutrinos near the inverted mass hierarchy region with KamLAND-Zen. *Phys. Rev. Lett.* 117, 082503. doi:10.1103/PhysRevLett.117.082503

Gavrilyuk, Y. M., Gangapshev, A. M., Kazalov, V. V., Kuzminov, V. V., Panasenko, S. I., Ratkevich, S. S., et al. (2015). A technique for searching for the 2K capture in^{124}Xe with a copper proportional counter. *Phys. Atomic Nucl.* 78, 1563–1566. doi:10.1134/S1063778815130098

González-Díaz, D., Álvarez, V., Borges, F., Camargo, M., Cárcel, S., Cebrián, S., et al. (2015). Accurate γ and MeV-electron track reconstruction with an ultra-low diffusion Xenon/TMA TPC at 10 atm. *Nucl. Instrum. Methods Phys. Res. Sect. A Accel. Spectrom. Detect. Assoc. Equip.* 804, 8–24. doi:10.1016/j.nima.2015.08.033

Gonzalez-Diaz, D., Monrabal, F., and Murphy, S. (2018). Gaseous and dual-phase time projection chambers for imaging rare processes. *Nucl. Instrum. Methods Phys. Res. Sect. A Accel. Spectrom. Detect. Assoc. Equip.* 878, 200–255. doi:10.1016/j.nima.2017.09.024

Henriques, C. , Amedo, P., Teixeira, J., González-Díaz, D., Azevedo, C., Para, A., et al. (2022). Neutral bremsstrahlung emission in xenon unveiled. *Phys. Rev. X* 12, 021005. doi:10.1103/PhysRevX.12.021005

Henriques, C. A. O. (2019). Studies of xenon mixtures with molecular additives for the NEXT electroluminescence TPC. Ph.D. thesis. Available online at: https://hdl.handle.net/10316/87464.

Henriques, C. A. O., Freitas, E., Azevedo, C., González-Díaz, D., Mano, R., Jorge, M., et al. (2017). Secondary scintillation yield of xenon with sub-percent levels of CO_2 additive for rare-event detection. *Phys. Lett. B* 773, 663–671. doi:10.1016/j.physletb.2017.09.017

Henriques, C. A. O., Monteiro, C. M. B., González-Díaz, D., Azevedo, C. D. R., Freitas, E. D. C., Mano, R. D. P., et al. (2019). Electroluminescence TPCs at the thermal diffusion limit. *J. High Energy Phys.* 2019, 027. doi:10.1007/JHEP01(2019)027

Henriques, C. A. O., Teixeira, J. M. R., Silva, P. A. O. C., Mano, R. D. P., dos Santos, J. M. F., and Monteiro, C. M. B. (2024). Understanding the xenon primary scintillation yield for cutting-edge rare event experiments. *J. Cosmol. Astropart. Phys.* 2024, 041. doi:10.1088/1475-7516/2024/06/041

Luscher, R., Farine, J., Boehm, F., Gabathuler, K., Gervascio, G., Lou, K., et al. (1998). Search for beta beta decay in Xe-136: new results from the gotthard experiment. *Phys. Lett. B* 434, 407–414. doi:10.1016/S0370-2693(98)00906-X

Mao, F. M., and Leck, J. (1987). The Quadrupole mass spectrometer in practical operation. *Vacuum* 37, 669–675. doi:10.1016/0042-207X(87)90053-4

Monteiro, C. M. B., Fernandes, L. M. P., Lopes, J. A. M., Coelho, L. C. C., Veloso, JFCA, Santos, J. M., et al. (2007). Secondary scintillation yield in pure xenon. *JINST* 2, P05001. doi:10.1088/1748-0221/2/05/P05001

Novella, P., Sorel, M., Usón, A., Adams, C., Almazán, H., Álvarez, V., et al. (2023). Demonstration of neutrinoless double beta decay searches in gaseous xenon with NEXT. *J. High Energy Phys.* 2023, 190. doi:10.1007/JHEP09(2023)190

Nygren, D. R. (2013). Columnar recombination: a tool for nuclear recoil directional sensitivity in a xenon-based direct detection WIMP search. *J. Phys. Conf. Ser.* 460, 012006. doi:10.1088/1742-6596/460/1/012006

Oliveira C., C., Sorel, M., Martin-Albo, J., Gomez-Cadenas, J., Ferreira, A., and Veloso, J. (2011). Energy resolution studies for NEXT. *J. Instrum.* 6, P05007. doi:10.1088/1748-0221/6/05/p05007

Oliveira C. A. B., Schindler, H., Veenhof, R., Biagi, S., Monteiro, C., dos Santos, J., et al. (2011). A simulation toolkit for electroluminescence assessment in rare event experiments. *Phys. Lett. B* 703, 217–222. doi:10.1016/j.physletb.2011.07.081

Renner, J., Díaz López, G., Ferrario, P., Hernando Morata, J. A., Kekic, M., Martínez-Lema, G., et al. (2019). Energy calibration of the NEXT-white detector with 1% resolution near $Q_{\beta\beta}$ of^{136}Xe. *J. High Energy Phys.* 2019, 230. doi:10.1007/JHEP10(2019)230

Renner, J., Farbin, A., Vidal, J. M., Benlloch-Rodríguez, J., Botas, A., Ferrario, P., et al. (2017). Background rejection in NEXT using deep neural networks. *JINST* 12, T01004. doi:10.1088/1748-0221/12/01/T01004

SAES (2025). SAES, st 707 pills and pieces. Available online at: https://www.saesgetters.com/products-functions/products/getters/non-evaporable-getters/pills-pieces (Accessed 01 January, 2023).

Simões, P. C. P. S., Covita, D. S., Veloso, JFCA, dos Santos, J. M. F., and Morgado, R. (2003). A new method for pulse analysis of driftless-gas proportional scintillation counters. *Nucl. Instrum. Methods Phys. Res. Sect. A Accel. Spectrom. Detect. Assoc. Equip.* 505, 247–251. doi:10.1016/s0168-9002(03)01062-3

Simões, P. C. P. S., Dos Santos, J. M. F., and Conde, C. A. N. (2001). Driftless gas proportional scintillation counter pulse analysis using digital processing techniques. *X-Ray Spectrom.* 30, 342–347. doi:10.1002/xrs.508

Simons, D. G., and de Korte, P. A. J. (1989). Soft X-ray energy resolution and background rejection in a driftless gas scintillation proportional counter. *Nucl. Instrum. Methods Phys. Res. Sect. A Accel. Spectrom. Detect. Assoc. Equip.* 277, 642–656. doi:10.1016/0168-9002(89)90799-7

Takahashi, T., Himi, S., Suzuki, M., RuanGen, J. z., and Kubota, S. (1983). Emission spectra from Ar–Xe, Ar–Kr, Ar–N2, Ar–CH4, Ar–CO2 and Xe–N2 gas scintillation proportional counters. *Nucl. Instrum. Methods Phys. Res.* 205, 591–596. doi:10.1016/0167-5087(83)90028-5

Teixeira, J. M. R., Henriques, C. A. O., Silva, PAOC, Mano, R. D. P., Dos Santos, J. M. F., and Monteiro, C. M. B. (2025). Efficient noble gas purification using hot getters and gas circulation by convection. *JINST* 20, C02026. doi:10.1088/1748-0221/20/02/C02026

Yan, X., Cheng, Z., Abdukerim, A., Bo, Z., Chen, W., Chen, X., et al. (2024). Searching for two-neutrino and neutrinoless double beta decay of Xe134 with the PandaX-4T experiment. *Phys. Rev. Lett.* 132, 152502. doi:10.1103/PhysRevLett.132.152502